Supplementary Information

Observation of Magnetoelectric Multiferroicity in a Cubic Perovskite System $LaMn_3Cr_4O_{12}$

Xiao Wang,[1,2] Yisheng Chai,[1] Long Zhou,[1] Huibo Cao,[3] Clarina-dela Cruz,[3] Junye Yang,[1] Jianhong Dai,[1] Yunyu Yin,[1] Zhen Yuan,[1] Sijia Zhang,[1] Runze Yu,[4] Masaki Azuma,[4] Yuichi Shimakawa,[5] Huimin Zhang,[6] Shuai Dong,[6] Young Sun,[1,*] Changqing Jin,[1,2] and Youwen Long[1,2,*]

[1]*Beijng National Laboratory for Condensed Matter Physics, Institute of Physics, Chinese Academy of Sciences, Beijing 100190, China*

[2]*Collaborative Innovation Center of Quantum Matter, Beijing 100190, China*

[3]*Quantum Condensed Matter Division, Neutron Scattering Science Directorate, Oak Ridge National Laboratory, Oak Ridge, Tennessee 37831, USA*

[4]*Materials and Structures Laboratory, Tokyo Institute of Technology, 4259 Nagatsuta, Midori-ku, Yokohama 226-8503, Japan*

[5]*Institute for Chemical Research, Kyoto University, Uji, Kyoto 611-0011, Japan*

[6]*Department of Physics, Southeast University, Nanjing 211189, China*

*Corresponding E-mail: ywlong@iphy.ac.cn; youngsun@iphy.ac.cn

In this Supplementary Material, we provide detailed information on the specific experimental and theoretical calculation methods adopted in this work, the possible influence of impurity phases on the intrinsic physical properties of LMCO, and the discussion on the magnetoelastic-coupling induced pyroelectric current as well as the possible local displacements of the B-site Cr ions in LMCO. In addition, low-temperature XRD, Raman and NPD patterns, magnetization, poling procedure dependence of electric behaviors and density functional theory (DFT) results as well as the data of crystal and magnetic structure refinements are provided in detail.

Experimental methods

The polycrystalline LMCO sample was prepared by a high-pressure and high-temperature method as described elsewhere [1]. The magnetic susceptibility and magnetization were measured by using a Quantum Design superconducting quantum interference device magnetometer. The pyroelectric current was measured with an electrometer (Keithley 6517B) while sweeping the temperature at a rate of 2 K/min before poled with ±100 V. The electric polarization was calculated by integrating I_p as a function of time. The dielectric constant was measured by an Agilent-4980A LCR meter. The XRD was performed by using a Rigaku diffractometer with Cu-Kα radiation. The NPD measurements were carried out using the constant wavelength (λ = 2.406 Å) high resolution

neutron powder diffractometer HB2a housed at the High Flux isotope reactor in Oka Ridge National Laboratory. The data refinements were completed by the Rietveld method with the FullProf program [2]. Raman scattering spectra were collected on a Renishaw Micro-Raman spectroscopy system in backscattering geometry.

Details of theoretical calculations

The DFT calculations were performed using the generalized gradient approximation with the Perdew-Becke-Erzenhof-revised (PBEsol) parameterization as implemented in the Vienna *ab initio* simulation package (VASP) [3-5]. The VASP version we used is 5.2.12. The PAW pseudo-potentials are the GGA ones: La, O, Mn_pv, and Cr_pv as provided by VASP. The electronic convergence criterion is 0.001 meV (EDIFF = 10^{-6}). To better describe the correlation effect, the Hubbard correlation item (U_{eff} = U - J) is taken into account all through the computational process [6], which is applied to Mn's *d* (4.0 eV) and Cr's *d* (3.0 eV) levels according to previous literature [7]. The plane-wave cutoff is 500 eV and a 7×7×7 Monkhorst-Pack *k*-point mesh centered at Γ point is adopted. There is no problem with La's *f*-states since their positions are much higher than the Fermi level for about 4 eV according to the projected density of states (see Supplementary Fig. S6). We know that in some case, a large U must be added to the *f*-states to push up their position [8], but here it is not necessary. The calculated density of states

with a band gap about 1.75 eV reveals the insulating nature of LMCO (Supplementary Fig. S6). The calculated local moments for Mn (3.907 μ_B) and Cr (2.799 μ_B) ions are also in agreement with the NPD refinement results (Supplementary Table S1).

The ferroelectric polarization is calculated using the Berry phase method [9]. The experimental magnetic orders are adopted and the structure is relaxed starting from the experimental one. With magnetism but without the spin-orbit coupling, the relaxed structure shows a cubic lattice whose lattice constant is very close to (only 0.26% larger than) the experimental one. The force criteria for structural relaxations are 3 meV/A (EDIFFG = -3×10^{-3}). The obtained lattice remains cubic, with a lattice constant as 7.41735 Å. For this relaxed structures, all La's, Mn's, and Cr's remain in their original high symmetric positions, and oxygen atoms are symmetrically arranged. Using this high symmetric structure, the calculation with spin-orbit coupling, can still give a finite polarization (3.4 $\mu C/m^2$) along the [111] axis when all spins are parallel/antiparallel to the [111] axis. By rotating these spin globally to the [-111] axis, the induced polarization can be switched, suggesting an intrinsic magnetism induced polarization.

When the inner ionic positions are further relaxed with spin-orbit coupling enabled, the force criteria for these relaxations are 5 meV/A (EDIFFG = -5×10^{-3}). Then the polarization is recalculated using this

relaxed structure, which gives 7.5 μC/m^2 along the [111] axis. Its order of magnitude and direction agree with the experimental observations.

Possible influence of impurities on the physical properties of LMCO

As seen from the XRD and NPD patterns (Supplementary Figs. S1 and S3), a small amount of Cr_2O_3 and $MnCr_2O_4$ impurity phases (< 5 wt%) was observed in our high-pressure product. Although these two phases exhibit multiferroic behaviors, they do not affect the intrinsic physical properties of LMCO. Specifically, Cr_2O_3 displays ME effect below 307 K [10], but this phase transition temperature is much different from T_{Mn} (= 50 K) and T_{Cr} (= 150 K) observed in our LMCO (Figs. 1c and 2a). Moreover, we do not find any visible polarization above 180 K (Figs. 2b and 2c), indicating that the magnetic and electric transitions as well as the ME coupling of LMCO are not related to Cr_2O_3 impurity. In addition, $MnCr_2O_4$ shows a sharp ferrimagnetic transition at 43 K and exhibits significant spontaneous magnetization with the saturated moment about 1.0 μ_B/f.u. at 5 K [11]. In our sample, however, we do not find any magnetic anomaly around 43 K (Fig. 2a), and the magnetic field dependence of magnetization shows a completely linear relationship at 5 K (Supplementary Fig. S4). Therefore, the effect of $MnCr_2O_4$ on the intrinsic physical properties of LMCO can also be safely ruled out.

Excluding of magnetoelastic-coupling induced pyroelectric current in

LMCO

Note that, recently, a centrosymmetric perovskite $SmFeO_3$ had been reported to have multiferroicity induced by noncollinear G-type antiferromagnetic order [12]. Unfortunately, however, this reported ferroelectricity was later disproved by theories [13] and other experiments [14]. Especially, Kuo *et al*. suggested that magnetoelastic coupling can give rise to artificial pyroelectric current as observed in $SmFeO_3$ [14]. However, it is not the case for our LMCO sample. The magnetoelastic-coupling induced pyroelectric current usually is not switchable by poling electric field, as pointed out by R. D. Johnson *et al*. for the case of $CaBaCo_4O_7$ [15]. However, the pyroelectric current of LMCO can be reversed by poling electric field. Moreover, the sign of magnetoelectric coefficient (dP/dH) can also be reversed by changing the direction of poling electric field. The above two facts can completely rule out the magnetoelastic-coupling mechanism in our sample. Therefore, the ferroelectricity in LMCO below T_{Mn} = 50 K should be intrinsic in origin.

Discussions on the possible local displacements of Cr ions in LMCO

To further explore the possible local displacements of Cr cations in the present LMCO, low-temperature Raman scattering was performed as presented in Supplementary Fig. S2. In agreement with NPD and XRD data, the low-temperature Raman spectra do not show any long-rang crystal structure phase transition with temperature down to 10 K.

However, some Raman peaks which reflect the vibrations of CrO_6 octahedra somewhat change the vibration frequency and the full width at half maximum around 180 K [16], maybe implying a local-structure origin for the FE2 phase. However, more experimental methods such as high-resolution neutron pair distribution function are needed to clarify the exact origin of FE2 phase.

References

[1] Y. W. Long, T. Saito, M. Mizumaki, A. Agui, and Y. Shimakawa, J. Am. Chem. Soc. **131**, 16244 (2009).

[2] J. Rodriguez-Carvajal, Physica B **192**, 55 (1993).

[3] P. E. Blöchl, O. Jepsen, and O. K. Andersen, Phys. Rev. B **49**, 16223 (1994).

[4] G. Kresse and J. Hafner, Phys. Rev. B **47**, 558 (1993).

[5] G. Kresse and J. Furthmüller, Phys. Rev. B **54**, 11169 (1996).

[6] S. L. Dudarev, G. A. Botton, S. Y. Savrasov, C. J. Humphreys, and A. P. Sutton, Phys. Rev. B **57**, 1505 (1998).

[7] S. Lv, H. Li, X. Liu, and J. Meng. J. Appl. Phys. **110**, 023711 (2011).

[8] R. L. Johnson-Wilke *et al*., Phys. Rev. B **88**, 174101 (2013).

[9] A. Iyama and T. Kimura, Phys. Rev. B **87**, 180408(R) (2013).

[10] N. Mufti *et al*., J. Phys.: Condens. Matter **22**, 075902 (2010).

[11] R. D. King-Smith and D. Vanderbilt, Phys. Rev. B **47**, 1651 (1993).

[12] J.-H. Lee, Y. K. Jeong, J. H. Park, M.-A. Oak, H. M. Jang, J. Y. Son,

and J. F. Scott, Phys. Rev. Lett. **107**, 117201 (2011).

[13] R. D. Johnson, N. Terada, and P. G. Radaelli, Phys. Rev. Lett. **108**, 219701 (2012).

[14] C.-Y. Kuo *et al*., Phys. Rev. Lett. **113**, 217203 (2014).

[15] R. D. Johnson, K. Cao, F. Giustino, and P. G. Radaelli, Phys. Rev. B **90**, 045129 (2014).

[16] N. Kolev *et al*., Phys. Rev. B **66**, 132102 (2002).

Supplementary FIG. S1. (a) Temperature dependent XRD patterns of $LaMn_3Cr_4O_{12}$. The diffraction peaks were indexed based on the space group of *Im*-3. The stars show the diffraction peaks originating from a small amount of Cr_2O_3 impurity. (b)-(e) The enlarged views for several representative diffractions peaks. No structural phase transition occurs as temperature decreases from 293 to 23 K.

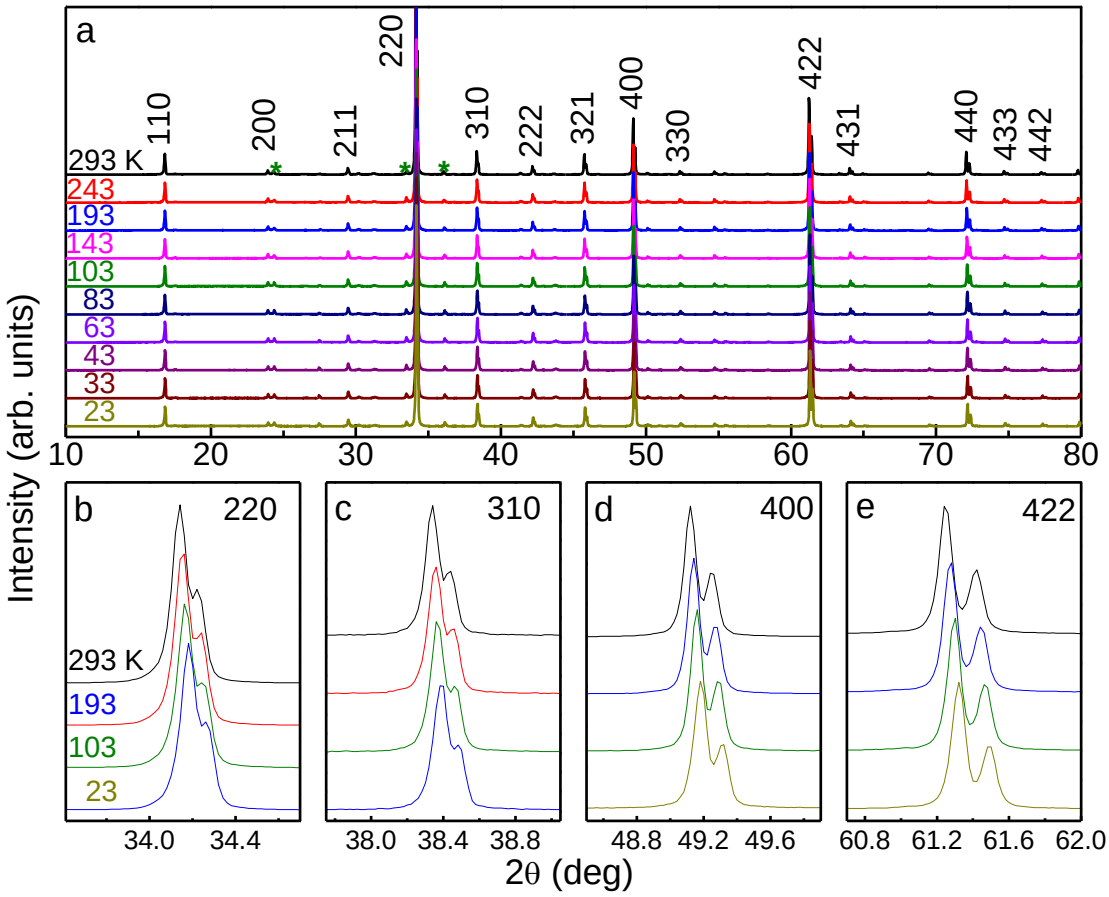

Supplementary FIG. S1

Supplementary FIG. S2. (a) Raman spectra measured at different temperatures for $LaMn_3Cr_4O_{12}$. No long-range structural phase transition is observed between 300 and 10 K. Temperature dependence of (b) Raman shift and (c) the full width at half maximum (FWHM) for the most two strong Raman modes $A_g(2)$ and $E_g(2)$. The anomalies occurred around 180 K may demonstrate some possible local structural displacements of Cr ions.

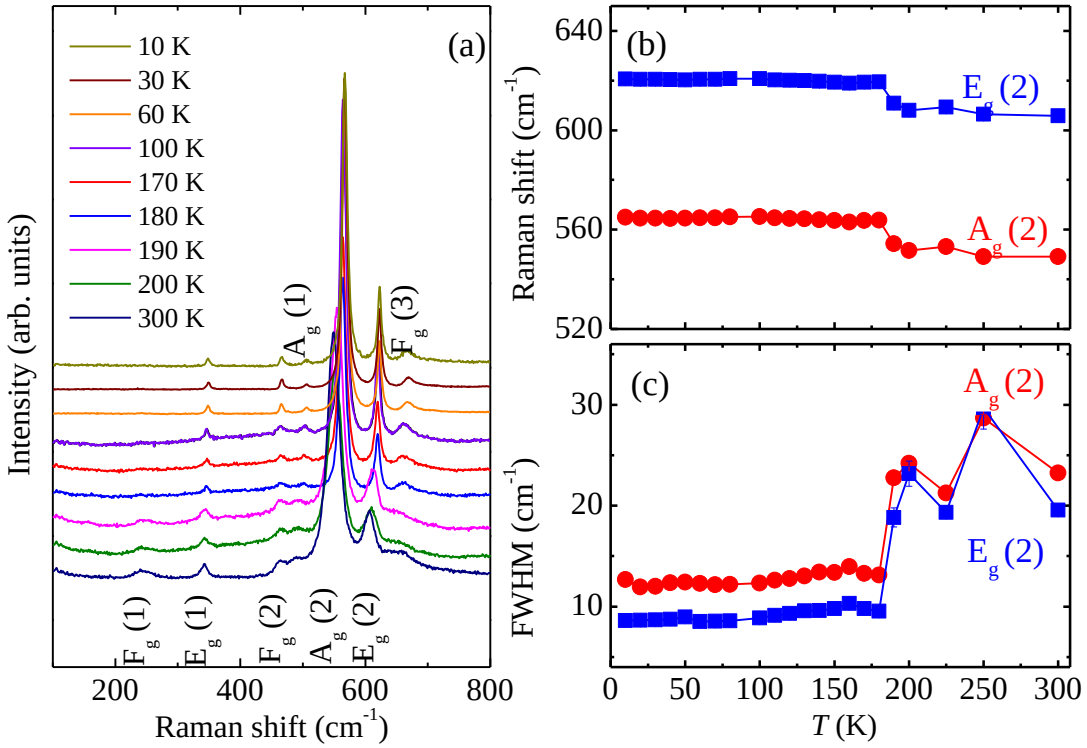

Supplementary FIG. S2

Supplementary FIG. S3. Rietveld refinements for the neutron powder diffraction data of $LaMn_3Cr_4O_{12}$ collected at (a) 170 K, (b) 80 K, (c) 35 K, and (d) 2 K. A small amount of Cr_2O_3 and $MnCr_2O_4$ impurity phases (< 5 wt%) was observed.

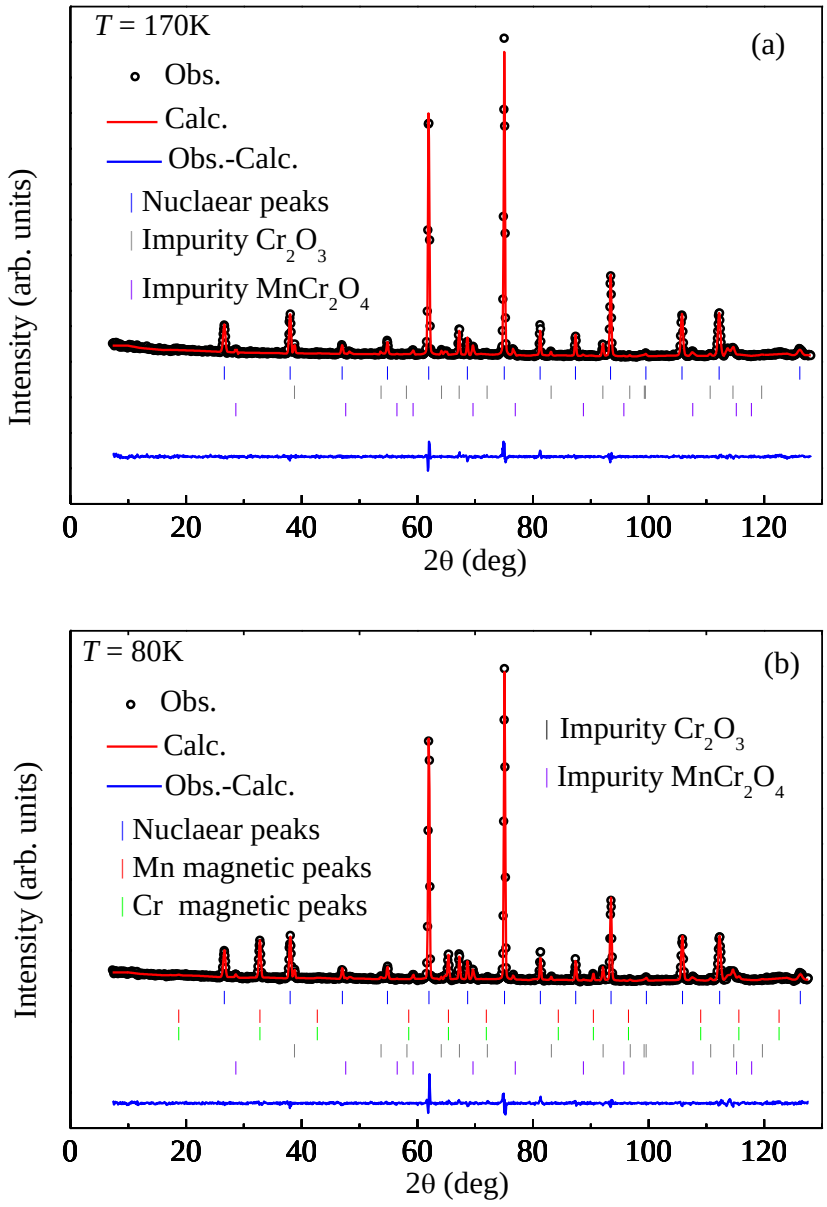

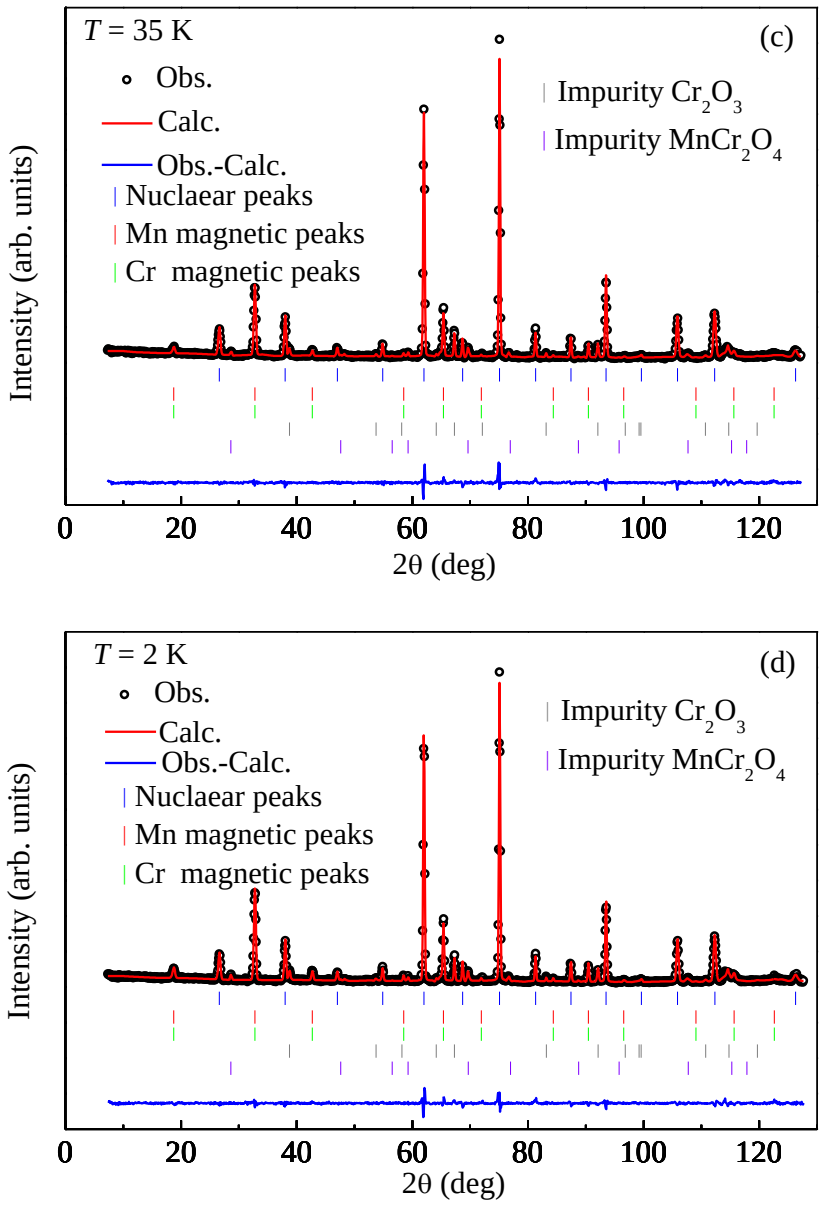

Supplementary FIG. S3

Supplementary FIG. S4. Magnetic field dependence of magnetization measured at different temperatures. The linear magnetization behaviors are consistent with the collinear G-type antiferromagnetic structure of $LaMn_3Cr_4O_{12}$ as revealed by neutron powder diffraction.

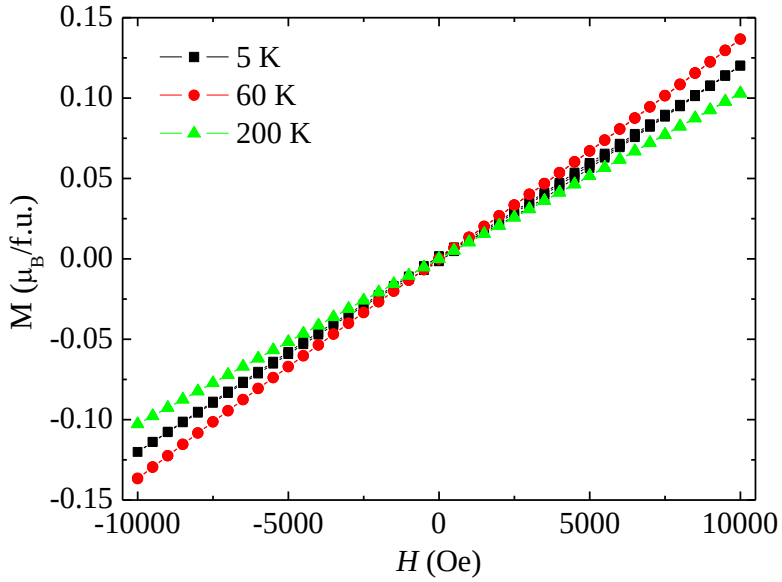

Supplementary FIG. S4

Supplementary FIG. S5. Poling procedure dependence of electric behaviors below T_{Mn}. (a) Temperature dependence of pyroelectric current I_p by +Poled and -Poled under 200-75 K and 75-30 K poling conditions. Temperature dependence of (b) I_p and (c) the difference of polarization ΔP (= $P(T)$ - P(50 K)) after being +Poled from 200 K down to the selected temperatures. The ΔP is obtained by integration of I_p in (b) as a function of time. As shown in (b), a dip-peak feature is observed when E passes through both 180 K and T_{Mn}, whereas only a single dip is observed when E is turned off at temperatures higher than T_{Mn}. Therefore, the dip in I_p at T_{Mn} should be contributed to FE2 phase, and the peak in I_p at T_{Mn} originates from the FE1 phase. The corresponding negative ΔP indicates that the electric polarization of the FE2 phase decreases in magnitude below T_{Mn}.

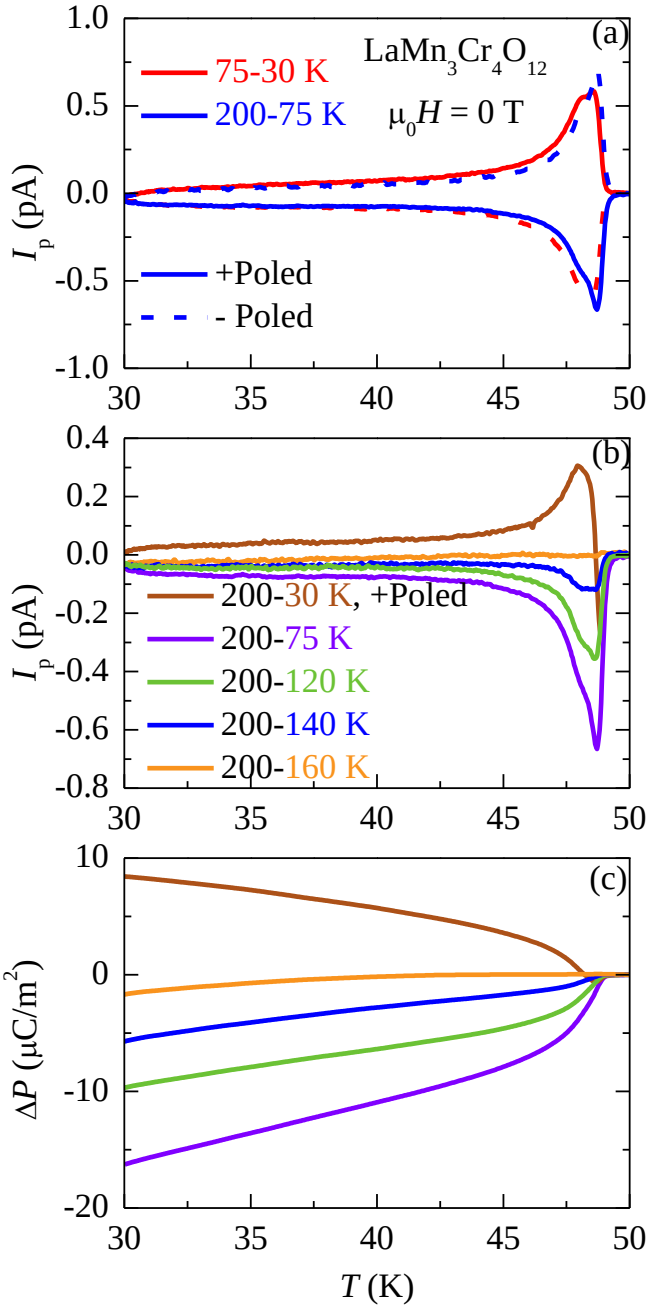

Supplementary FIG. S5

Supplementary FIG. S6. DFT results with the dual G-type antiferromagnetism (without SOC). Projected density of states (PDOS) for each atom species is shown. The calculated band gap (~1.75 eV) reveals the insulating nature of $LaMn_3Cr_4O_{12}$.

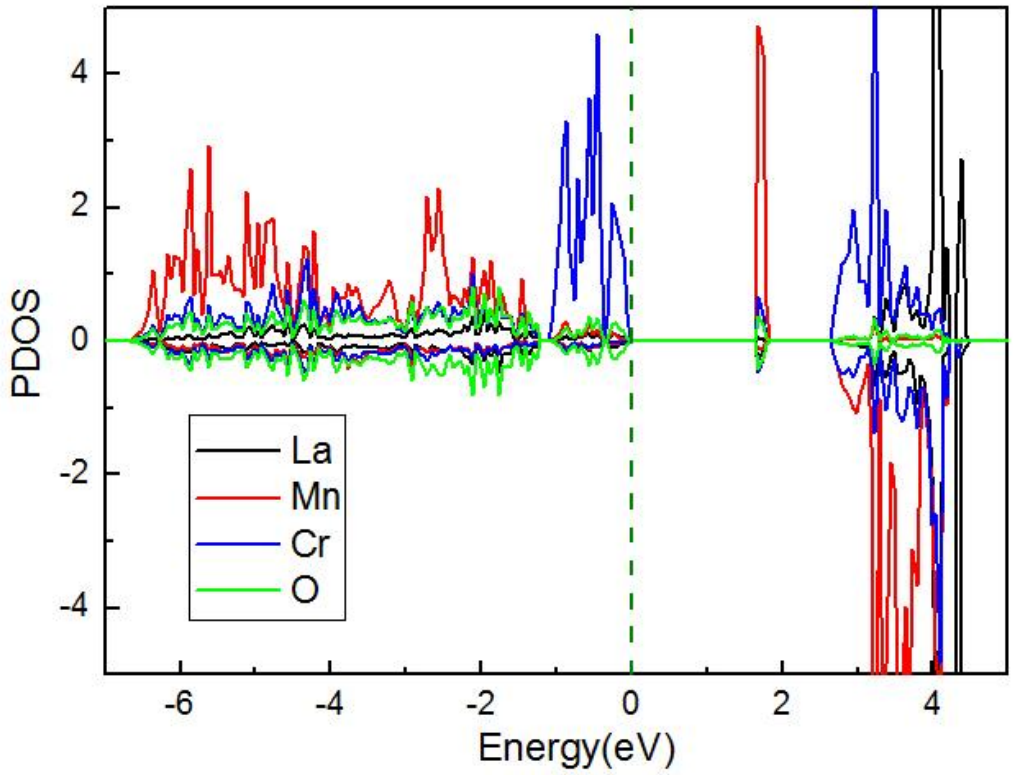

Supplementary FIG. S6

Supplementary Table S1. Refined structural parameters for the neutron powder diffraction data of $LaMn_3Cr_4O_{12}$ at different temperatures. The space group is *Im*-3 (No. 204). In this structure model, the A-site La and A′-site Mn cations are 1:3 ordered in special atomic positions 2*a* (0, 0, 0) and 6*b* (0, 0.5, 0.5), respectively. The B-site Cr atom occupies the special 8*c* (0.25, 0.25, 0.25) site, and the O atom locates at the 24*g* (0, *y*, *z*) site.

Structural parameters	2 K	35 K	80 K	170 K
a (Å)	7.39805(9)	7.3988(1)	7.3996 (1)	7.4028(1)
y (O)	0.3104(4)	0.3096(4)	0.3099(4)	0.3102(3)
z (O)	0.1771(4)	0.1765(5)	0.1767 (4)	0.1757(4)
U_{iso} (O)	0.004(2)	0.004(2)	0.004(2)	0.004(2)
U_{iso} (La)	0.009(3)	0.005(3)	0.008(3)	0.009(3)
U_{iso} (Mn)	0.040(3)	0.036(3)	0.037(3)	0.032(3)
U_{iso} (Cr)	0.054(3)	0.055(3)	0.048(3)	0.048(3)
$d_{Mn\text{-}O}$ (Å) (×4)	1.919(3)	1.921(3)	1.921(3)	1.915(2)
$d_{Cr\text{-}O}$ (Å) (×6)	1.978(3)	1.978(4)	1.978(3)	1.981(5)
$d_{La\text{-}O}$ (Å) (×12)	2.644(3)	2.637(3)	2.639(3)	2.639(1)
$\angle_{Cr\text{-}O\text{-}Cr}$ (°)	138.52(4)	138.54(5)	138.55(4)	138.14(4)
M_{Mn} (μ_B)	3.40(8)	2.66(9)	0	0
M_{Cr} (μ_B)	2.89(6)	2.81(6)	2.50(3)	0
R_{Bragg} (%)	1.60	3.70	2.79	2.88